ESCRT-mediated vesicle concatenation in plant endosomes

Rafael Andrade Buono,[1,2*] André Leier,[7,8*] Julio Paez-Valencia,[1,2*] Janice Pennington,[9] Kaija Goodman,[1,2] Nathan Miller,[1] Paul Ahlquist,[3,4,5,9,10] Tatiana T. Marquez-Lago,[7,8] and Marisa S. Otegui[1,2,6]

[1]Department of Botany, [2]R.M. Bock Laboratories of Cell and Molecular Biology, [3]Institute for Molecular Virology, [4]Departments of Oncology, [5]Department of Plant Pathology, and [6]Department of Genetics, University of Wisconsin-Madison, Madison, WI
[7]Informatics Institute, School of Medicine and [8]Department of Genetics, School of Medicine, University of Alabama at Birmingham, Birmingham, AL
[9]Howard Hughes Medical Institute, Chevy Chase, MD
[10]Morgridge Institute for Research, Madison, WI

Ubiquitinated plasma membrane proteins (cargo) are delivered to endosomes and sorted by endosomal sorting complex required for transport (ESCRT) machinery into endosome intralumenal vesicles (ILVs) for degradation. In contrast to the current model that postulates that ILVs form individually from inward budding of the endosomal limiting membrane, plant ILVs form as networks of concatenated vesicle buds by a novel vesiculation mechanism. We ran computational simulations based on experimentally derived diffusion coefficients of an ESCRT cargo protein and electron tomograms of *Arabidopsis thaliana* endosomes to measure cargo escape from budding ILVs. We found that 50% of the ESCRT cargo would escape from a single budding profile in 5–20 ms and from three concatenated ILVs in 80–200 ms. These short cargo escape times predict the need for strong diffusion barriers in ILVs. Consistent with a potential role as a diffusion barrier, we find that the ESCRT-III protein SNF7 remains associated with ILVs and is delivered to the vacuole for degradation.

Introduction

Vesicle trafficking pathways are highly regulated processes that require specific machineries to select vesicle cargo, deform and fission membranes, and mediate the transport and fusion of the resulting vesicle with the acceptor compartment. The initial sorting and clustering of cargo macromolecules in a vesicle require their concentration in a small region of the donor membrane. In the case of clathrin-mediated endocytosis and the anterograde and retrograde trafficking between the endoplasmic reticulum and Golgi via COP-II and COP-I vesicles, respectively, the cargo molecules directly or through adapters recruit a protein coat that aids in the local deformation of the membrane into a bud (Traub and Bonifacino, 2013; Gomez-Navarro and Miller, 2016). The cargo remains physically associated with these coats after the vesicle is free in the cytoplasm and until the coat disassembles, greatly limiting the possibility of cargo escape back to the donor membrane by diffusion during vesicle formation.

The degradation of plasma membrane proteins depends on different membrane vesiculation events along the endocytic and endosomal pathways. At the plasma membrane, linear amino acid motifs, conformational motifs, and/or posttranslational modifications such as phosphorylation and ubiquitination of plasma membrane proteins are recognized by adapter and accessory proteins (Traub and Bonifacino, 2013) that also facilitate the assembly of the clathrin coat and the formation of endocytic vesicles. Once released from the plasma membrane, clathrin-coated vesicles lose their coats and fuse with endosomes. At endosomes, the endocytosed cargo proteins can be recycled back to the plasma membrane or internalized into endosomal intralumenal vesicles (ILVs) for their degradation upon the fusion of multivesicular endosomes (MVEs) with vacuoles/lysosomes (Henne et al., 2011). The major sorting signal for endosomal-mediated vesiculation is ubiquitin (MacDonald et al., 2012). Ubiquitinated cargo proteins on the endosomal limiting membrane are recognized and sorted into ILVs by endosomal sorting complex required for transport (ESCRT) proteins (Schuh and Audhya, 2014; Paez Valencia et al., 2016).

The ESCRT machinery mediates negative membrane bending (away from the cytoplasm), leading to a vesiculation process in the reverse topology to most membrane-deformation events, including clathrin-coated endocytosis. In fungi and metazoans, five multimeric ESCRT complexes have been identified (ESCRT-0, -I, -II, and -III and VPS4-VTA1; Henne et

*R.A. Buono, A. Leier, and J. Paez-Valencia contributed equally to this paper.

Correspondence to Marisa S. Otegui: otegui@wisc.edu

R.A. Buono's present address is Dept. of Plant Systems Biology, Vlaams Instituut voor Biotechnologie, Ghent University, Ghent, Belgium.

Abbreviations used: ESCRT, endosomal sorting complex required for transport; ILV, intralumenal vesicle; MSD, mean square displacement; MVE, multivesicular endosome; TIRFM, total internal reflection fluorescence microscopy.

The Rockefeller University Press
J. Cell Biol. Vol. 216 No. 7 2167–2177
https://doi.org/10.1083/jcb.201612040

al., 2011; Hurley, 2015). ESCRT-0, -I, and -II contain ubiquitin-binding domains that interact with the ubiquitinated cargo proteins, contributing to the clustering of cargo on endosomal membranes. The ESCRT-III subunit VPS32/Snf7p is known to assemble into long spiral filaments and induce membrane curvature (Shen et al., 2014; Chiaruttini et al., 2015). Although ESCRT-III does not seem to bind ubiquitin, the ESCRT-III spirals could have a critical role in corralling the ESCRT cargo at the endosomal membrane (Henne et al., 2012; Chiaruttini et al., 2015). However, whether the membrane-associated ESCRT-III spirals would serve as barriers, crowding cargo molecules and preventing their escape by lateral diffusion, has not been demonstrated. Moreover, deubiquitinating enzymes remove the ubiquitin on cargo proteins before the ILVs are released into the endosomal lumen (Richter et al., 2007, 2013; Johnson et al., 2017). This means that, in contrast with other types of coat-mediated vesiculation (e.g., clathrin-mediated endocytosis), the ESCRT coat loses direct contact with the cargo proteins before completion of vesicle formation. In addition, the ESCRTs are assumed to be removed from the ILV neck before membrane fission and recycled back to the cytoplasm (Babst et al., 2002). This raises the question of what prevents cargo proteins from diffusing away from the ILV buds.

Once the ESCRT-III complex is recruited by ESCRT-II onto the endosomal membranes, the ESCRT-III subunit VPS2 recruits the AAA ATPase VPS4, leading to the constriction of the budding ILV neck into a 17-nm-wide tubule, ESCRT disassembly, membrane fission, and ILV release into the endosomal lumen (Obita et al., 2007; Adell et al., 2014). Electron microscopy and electron tomographic analyses of yeast and mammalian MVEs have repeatedly shown single ILVs inside the MVE lumen (Murk et al., 2003a; Wemmer et al., 2011; Adell et al., 2014), supporting the notion that ILVs form one by one from single budding events by the sequential action of multiple ESCRT components. However, exactly how ESCRT proteins mediate ILV formation is unclear. A study of SNF7 polymers on membranes suggests that ESCRT-III spirals become loaded springs because of lateral compression from adjacent filaments, and their relaxation could lead to membrane deformation and ILV bud formation (Chiaruttini et al., 2015). VPS4 could further modify the architecture of the ESCRT-III polymers assisting in membrane constriction (Adell et al., 2014; Shen et al., 2014). Interestingly, although the SNF7 filaments are highly flexible and can grow at different radii, the smallest radius reported for SNF7 spirals is 18 nm (Chiaruttini et al., 2015), which is 10 times larger than the radius of the superconstricted, prefission state of dynamin polymers (Sundborger et al., 2014) that lead to membrane fission. This indicates that although SNF7 could trigger ILV bud formation, it may not by itself mediate pore closure and ILV release.

ESCRT proteins are present from archaea to eukaryotes. Plants contain orthologues for most of the ESCRT proteins, with the exception of the canonical ESCRT-0 (Winter and Hauser, 2006; Leung et al., 2008) together with plant-specific ESCRT components (Paez Valencia et al., 2016). In this study, we report on the occurrence of ILV concatenation in plant endosomes as a novel mechanism of vesicle formation as well as on the participation of ESCRT-III proteins in this process. We also analyze the effect of prerelease ILV membrane geometry on the potential escape time of deubiquitinated ESCRT cargo during the formation on ILVs by computational simulations based on electron tomograms of plant MVEs. Finally, and consistent with the presence of a persistent diffusion barrier in ILV networks predicted by our simulations, we show that SNF7 remains associated with internalized endosomal membranes after ILV release and fusion of MVEs with the vacuole.

Results

ILVs form as part of concatenated networks within MVEs

To understand changes in membrane geometry during endosomal vesiculation, we analyzed dual-axis electron tomograms of plant MVEs (32 MVEs from wild-type *Arabidopsis thaliana* root epidermal and cortical cells) and found that most ILVs (71%; sample size, 183 ILVs) do not form individually but as large networks of concatenated budding profiles (Fig. 1, A–F; and Video 1). We observed linear chains of vesicle buds interconnected through axial narrow membrane bridges or more complex networks of up to 12 ILV buds connected through both lateral and axial bridges (Fig. 1, C–F; and Video 1). Most of these networks were still connected to the limiting membrane by a nascent ILV bud with a narrow neck similar in size to that of inter-ILV bud bridges (mean width, 17 nm; SD, 1.5 nm; sample size, 25 bridges/necks; Fig. 1, A–F). We also obtained electron tomograms of MVEs from another plant cell type, root meristematic cells, and found similar networks of concatenated ILVs (Fig. S1, A and A'), suggesting that this is a common structural feature of plant MVEs. These observations are hard to reconcile with the current model that postulates that all ILVs are free in the MVE lumen (Murk et al., 2003b) and form one at a time when ESCRT-III and VPS4 pinch off the membrane at the bud neck. How, then, do these concatenated vesicles form? For the linear vesicle chain configuration, we considered two possible models. Once the first necked membrane bud is established, the second one forms either by initiation of further budding from the distal end of the same bud or by deformation of the limiting membrane above the first. We found multiple intermediates consistent with the second model (Fig. 1, G and H; and Fig. S1 C), suggesting that the first ILV bud to form in a linear concatenated chain is the one furthest away from the limiting membrane.

We also found geometries showing that single ILV buds in close proximity to each other were connected laterally through narrow membrane bridges (Fig. 1, I–I"). We were unable to find early intermediates showing whether these membrane connections derive from initial fusion of ILV buds followed by membrane bridge stabilization or if they are established simultaneously with ILV bud formation.

To determine whether ILV bud concatenation is also observed in other organisms besides plants, we obtained dual-axis electron tomograms of MVEs from high-pressure–frozen freeze-substituted *Saccharomyces cerevisiae* cells. Interconnected ILVs were detected in very low frequencies (6% concatenated ILVs; sample size, 65 ILVs) in yeast cells (Fig. S1, C–E), suggesting that either ILV networks are very short-lived or that ILVs do not form from a process of membrane bud concatenation as frequently as observed in plant cells.

To test whether ESCRT-III and other late ESCRT components are required for ILV concatenation, we obtained dual-axis electron tomograms of MVEs from *Arabidopsis* mutants lacking either the ESCRT-III subunits CHMP1A and B (Did2p in yeast) or the positive VPS4 regulator LIP5 (Vta1p

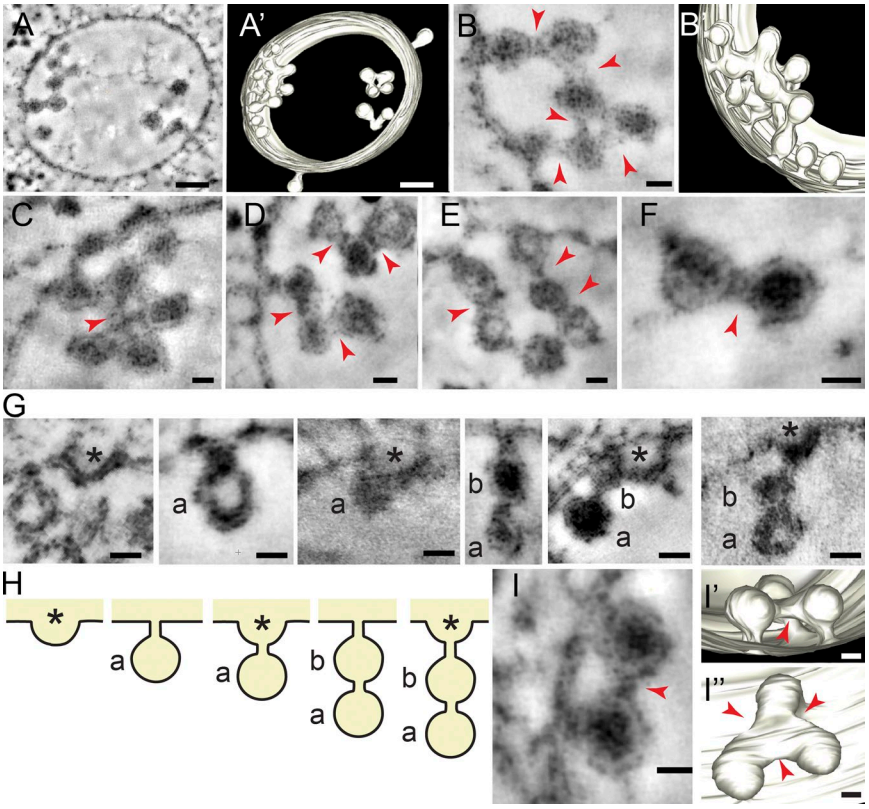

Figure 1. **Structural analysis of ILV formation.** (A and A′) Tomographic slice (A) and corresponding tomographic reconstruction (A′) of a wild-type MVE from a root cell. (B and B′) Tomographic slice (B) and tomographic reconstruction (B′) of the MVE depicted in A and A′, showing a detail of the concatenated network of ILV buds connected through narrow membrane bridges. (C–F) Tomographic slices from plant MVEs showing examples of concatenated ILV bud networks connected to the endosomal limiting membrane. (G) Tomographic slices showing intermediates in the process of ILV bud concatenation. Shallow invaginations corresponding with early stages in ILV bud formation are marked by asterisks; "a" indicates the first ILV to form, and "b" the second one. (H) Model of ILV bud concatenation based on the images depicted in G. (I–I″) Tomographic slice (I) and corresponding tomographic reconstruction (I′ and I″) of three ILV buds connected by lateral membrane bridges. Red arrowheads indicate interconnecting membrane bridges. Bars: (A and A′) 50 nm; (B–I″) 20 nm.

in yeast). These mutants, *chmp1* and *lip5*, are unable to efficiently sequester cargo into ILVs (Spitzer et al., 2009; Buono et al., 2016). We found that, compared with wild type, both *chmp1* and *lip5* MVEs had a lower density of ILVs, with a smaller proportion of concatenated ILV buds and significantly smaller ILV bud networks (Fig. 2, A–H; and Videos 2 and 3). In addition, we found that in some *chmp1* MVEs, concatenated ILV buds were connected to the limiting membrane by very long (~45 nm) necks (Fig. 2 D), suggesting a defect in the sequential formation of ILV buds that leads to ILV bud concatenation. Thus, the analysis of plant ESCRT mutant MVEs showed a correlation between ILV bud concatenation and efficient ILV formation.

Simulation of ESCRT cargo diffusion during ILV formation

ESCRT proteins are known to bind ubiquitin on cargo proteins. We have very little information about the extent to which ESCRT-III proteins can bind cargo directly and whether other proteins, such as the yeast tetraspan Cos proteins (MacDonald et al., 2015), can assist in ESCRT cargo sorting in plant cells. However, it is reasonable to assume that most of the deubiquitinated cargo molecules that arise after ESCRT-III assembles and before ILV release (Richter et al., 2007, 2013; Johnson et al., 2017) may not be physically connected to the ESCRT coat, and thus could diffuse away from the forming vesicle. Moreover, the escaped cargo molecules cannot be retrieved by the ESCRTs unless they are ubiquitinated again. This means that cargo sequestration into ILVs needs to be extremely efficient and that ILV release needs to be completed before cargo molecules can escape by diffusion. To determine whether the novel vesiculation mechanism that operates in plant MVEs could affect endosomal cargo entrapment, we performed computational simulations of cargo escape in single and concatenated ILV buds based solely on cargo lateral diffusion and membrane geometry.

We first calculated the diffusion coefficient of a known ESCRT cargo in plants, the auxin efflux facilitator PIN2 (Spitzer et al., 2009), by two imaging methodologies, single-particle tracking by total internal reflection fluorescence microscopy (TIRFM) and FRAP. Because it is extremely challenging to measure the diffusion of membrane proteins in the highly mobile endosomes, we measured diffusion of PIN2 fused to the photoconvertable tag EosFP (for TIRFM measurements) or to GFP (for FRAP measurements) in the plasma membrane of plant cells devoid of cell walls (protoplasts) as a proxy for PIN2 diffusion on MVE membranes (Videos 4 and 5).

Based on the tracking of photoconverted PIN2-EosFP particles in protoplasts, we estimated their diffusion coefficient to be 0.06 $\mu m^2/s$ (Figs. 3 A and S2). Using FRAP of protoplasts expressing PIN2-GFP, we estimated the diffusion coefficient of PIN2-GFP to be 0.17 $\mu m^2/s$ (Fig. 3 B). Similar discrepancies in diffusion coefficients calculated by FRAP or TIRFM have been reported previously for other plasma membrane proteins and may be explained by the fact that FRAP measurements can overestimate lateral diffusion by not considering that part of the fluorescence recovery is because of secretion (Ghosh et al., 2014). Regardless of this discrepancy, the diffusion coefficients obtained for fluorescently tagged PIN2 are within the range of what has been reported for other multispanning membrane proteins in animal and plant cells (Martinière et al., 2012; Oyola-Cintrón et al., 2015; Wang et al., 2016) and are useful estimates of the lateral diffusion of a potentially wide range of ESCRT cargo proteins.

To ensure that the model's physical properties of the simulated diffusion mimic the endosomal environment, we obtained dual-axis electron tomograms from *Arabidopsis*

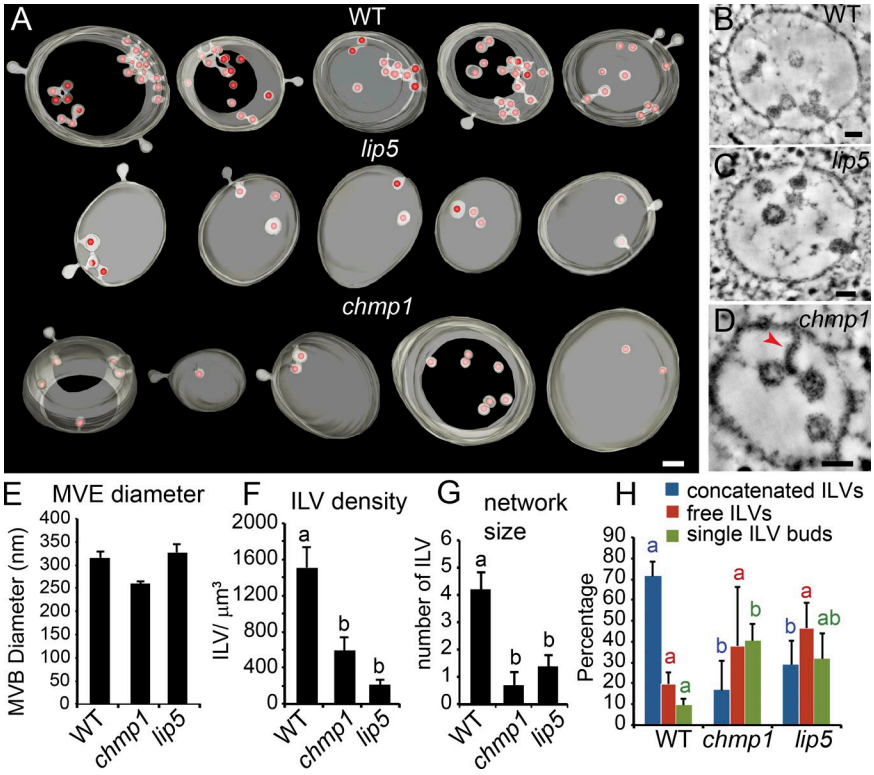

Figure 2. **Electron tomography of wild-type and ESCRT mutant MVEs from *Arabidopsis*.** (A) Tomographic reconstructions of dual-axis tomograms of wild-type, *chmp1*, and *lip5* mutant MVEs. Red spheres were placed inside ILV and ILV buds to facilitate their identification. Note the reduced number of ILVs and the limited ILV concatenation in mutant MVEs. (B–D) Tomographic slices of WT, *lip5*, and *chmp1* MVEs. The red arrowhead in D indicates a long neck connecting two concatenated ILV buds with the limiting membrane. Bars: (A) 50 nm; (B–D) 20 nm. (E–H) Quantitative analyses of MVE structural features. Error bars indicate SEM. Letters above bars represent statistical significance (one-way ANOVA followed by Tukey's test: $P < 0.05$); bars sharing a letter are not significantly different from one another. n = 11 (wild type), 7 (*chmp1*), and 11 (*lip5*) MVEs; n = 183 (wild type), 27 (*chmp1*), and 162 (*lip5*) ILVs.

MVEs and identified multiple membrane-inward ILV budding events. As cargo deubiquitination is assumed to happen after full assembly of ESCRT-III but before membrane scission (Johnson et al., 2017), we chose those geometries that corresponded with late ILV formation stages (i.e., narrow necks), segmented the cytoplasmic leaflet of the endosomal membrane (Figs. 3 C and S3), and adopted a diffusion model using a particle-based spatial stochastic simulator. Aside from the vesicle geometry, the basic model required specification of the size of the PIN2 molecules, their diffusion constant, the time step of the simulator, and a criterion for measuring exit times. We used three vesicle geometries from tomography reconstructions (Figs. 3 D and S3). Each geometry was divided into four regions: the lower and upper hemisphere of the vesicle, the endosomal limiting membrane, and the neck that connects the upper hemisphere with the endosomal limiting membrane (Figs. 3 D and S3). PIN2 molecules were initially placed at the lower hemisphere, creating a worst-case scenario for each molecule to exit the vesicle. As we were interested in escape times to the endosomal limiting membrane, PIN2 reentering the vesicle membrane from the endosomal surface was not possible in the model; once a PIN2 molecule moved to the endosomal limiting membrane, it was removed via a location-specific degradation reaction with probability 1. This is further justified by the consideration that the area of the limiting endosomal membrane is so large in comparison to that of the vesicle that the chance of the protein diffusing back once it escaped is very low. Consequently, reducing the endosomal surface to a small environment around the vesicle neck was sufficient for our modeling goal and reduced computing time. Escape times were then obtained from PIN2 decay over time.

For obtaining a reasonable, maximal number of PIN2 in the vesicle membrane, we considered that PIN2 is predicted to contain 10 α helices as transmembrane domains (UniProt database accession no. Q9LU77; Liu et al., 2014). The diameter of a transmembrane domain is ∼1.5 nm (Rosenberg et al., 2003), and thus the overall area covered by all PIN2 transmembrane domains was calculated to be 17.67 nm^2. Therefore, we roughly estimated the membrane area effectively covered by a PIN2 molecule at 20 nm^2. Based on the dimension of budding profiles (inner diameter, 23 nm; SD, 3 nm; sample size, 183 ILVs) in tomographic reconstructions of plant MVEs, we estimated that 41 PIN2 molecules could fit in the lower hemispheric region of the forming ILV (∼830 nm^2). We modeled the diffusion of 40 PIN2 molecules covering a circular area (Video 6). To estimate changes in escape time according to variations in protein diffusion, we ran simulations for the two experimentally calculated diffusion coefficients, 0.17 µm^2/s (D1) and 0.06 µm^2/s (D2). The spatial resolution was initially set to 0.715 nm, the pixel size of the tomography dataset. The simulation time step that guarantees such spatial resolution was then calculated as $\Delta t = s^2/4D$. Because the spatial unit of the imported geometries was in px, we chose to convert all parameters into the unit system px-ms. Simulations stopped when >10 PIN2 molecules were left in the vesicle. To account for steric effects in particle movement such as crowding effects and collisions, we also simulated PIN2 diffusion with volume exclusion. Based solely on diffusion, the 50% PIN2 escape time in simulation with no steric effects was between 10 ms (D1) and 28 ms (D2) (Figs. 3 E and S3), whereas with excluded-volume effects, PIN2 escape times decreased to 5 ms (D1) and 15 ms (D2; Fig. 3 F). This is consistent with theoretical models showing that lateral diffusion of particles with no electrostatic or hydrodynamic interactions is enhanced when steric effects are included (Bruna and Chapman, 2012). We also ran simulations for two additional ILV bud geometries at spatial resolutions of 0.715 nm or 1.43 nm (Fig. S3). Simulations in all ILV profiles yielded similar PIN2 escape dynamics (Fig. 3, E and F; and Fig. S3), confirming that minor geometric

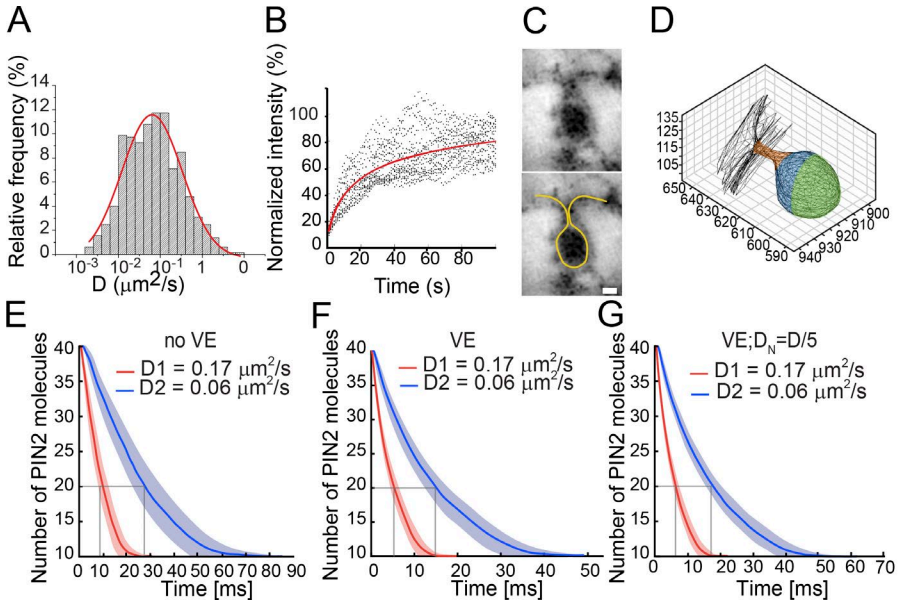

Figure 3. **Calculation of diffusion coefficients and escape times for PIN2.** (A) Distribution of diffusion coefficients (*D*) for PIN2-EosFP on the plasma membrane of fresh protoplasts (n = 648 tracks from four protoplasts) in a histogram with logarithmically spaced bins. The data were fitted using a Gaussian distribution (red curve). Single-particle tracks of PIN2-EosFP on the plasma membrane of protoplasts were visualized by TIRFM and used to calculate MSD. *D* values were calculated by linear fit to MSD versus time. (B) Quantitative FRAP experiments of 16 protoplasts to determine diffusion coefficient of PIN2-GFP. Fluorescence intensities during recovery after photobleaching are plotted versus time. (C) Electron tomography slice of a single ILV bud from an *Arabidopsis* root cell. The yellow line indicates the position of the contour used to segment the ILV bud in IMOD. Bar, 10 nm. (D) Extracted 3D geometry from the segmented ILV bud shown in C and used to run the simulations shown in E–G. Green indicates the lower ILV hemisphere, orange indicates the ILV bud neck, and blue indicates the rest of the ILV bud membrane. Numbers shown in nanometers. (E–G) Simulated escape times of 40 PIN2 particles placed on the lower hemisphere of the ILV bud using the two *D* values experimentally calculated by TIRFM (0.06 μm²) and by FRAP (0.17 μm²). The colored lines indicate the mean numbers of remaining cargo over time calculated from >300 simulations, and the shaded regions correspond with the SD. Gray vertical lines indicate the mean time required for 50% of the PIN2 particle to escape the ILV bud. Simulations were run either without (E) or with (F) volume exclusion and with a fivefold decrease in *D* when PIN2 particles entered the neck region (G). VE, volume exclusion.

differences or different resolutions do not significantly alter the simulations of diffusive behavior and escape times of PIN2.

To account more accurately for local changes in particle mobility caused by membrane geometry, we considered the narrow 17-nm-wide neck connecting the body of the vesicle bud to the endosomal limiting membrane. The mobility of the potassium-gated channel KvAP with six transmembrane domains (Lee et al., 2005) was shown to be reduced fivefold in ∼10-nm-wide membrane tubes compared with the diffusion in relatively flat membranes (Domanov et al., 2011). Therefore, we applied a fivefold reduction in the diffusion coefficient to all PIN2 particles entering the neck region in our simulations. We found that under these conditions, the 50% PIN2 escape time was between 7 ms (D1) and 18 ms (D2; Fig. 3 G). It is important to note, however, that the effect of the neck region on cargo diffusion depends on the size, geometry, and mechanical properties of the cargo proteins. Thus, the diffusion retardation effect in the neck regions could be more than fivefold for PIN2 but also less than fivefold for smaller cargo proteins with only one transmembrane-spanning region.

Vesicle concatenation and ESCRT cargo diffusion

Although ILVs in plant MVEs should be ultimately released into the endosomal or vacuolar lumen for degradation, early ILV bud concatenation could contribute to cargo entrapment while the forming ILV buds remain connected to the limiting membrane. For example, the concatenated ILV bud membranes would be still in contact with the cytoplasm, allowing for cargo deubiquitination, and therefore free cargo diffusion could only start once large and complex ILV networks have formed, greatly reducing the chances of cargo escape. To test this hypothesis in silico, we ran simulations of cargo escape through geometries of two or three concatenated ILV buds (Fig. 4, A and B). Because our electron tomography analysis indicated that the ILV furthest away from the limiting membrane is the first one to form, we placed 40 PIN2 molecules in the hemisphere for the ILVs deepest into the endosomal lumen. Most likely, ESCRT cargo is also found in the other regions of internalized membranes, but we restricted the simulation to the PIN2 pool that would be sequestered earlier when the first ILV bud formed. Because the ILV bud necks and interconnecting bridges between ILVs were similar in diameter, we applied the same fivefold reduction to the PIN2 particles moving into both regions. Compared with simulations on a single ILV bud, PIN2 escape times increased approximately fivefold for two concatenated ILVs and 10-fold for three concatenated ILVs (Fig. 3 B).

To fully appreciate the meaning of these calculated escape times, it would be critical to know how fast ILVs form. Unfortunately, because endosomes are highly mobile within cells, it is very challenging to measure the timing of ILV formation. However, we know that in animal cells, conventional clathrin-mediated vesiculation at the plasma membrane takes typically 10–20 s (Heuser and Reese, 1973), the entry of Singapore grouper iridovirus virions by endocytosis takes 1 s (Pan et al., 2015), and ultrafast endocytosis at hippocampal synapses proceeds in 50–100 ms (Watanabe et al., 2013). Given the relatively slow speed of such vesiculation events, the increased complexity of the ILV bud network geometry could delay cargo escape, but it does not seem to be sufficient to trap the cargo efficiently. Thus, even if endosome intralumenal vesiculation is as fast as the fastest vesiculation event ever recorded (ultrafast endocytosis), regardless of the mechanism by which ILVs forms (either by single or concatenated budding events), they would have lost most of their cargo by the time they detached from the endosomal membrane. Thus, our simulations predict the presence of additional diffusion barriers within endosomes to trap cargo within ILVs.

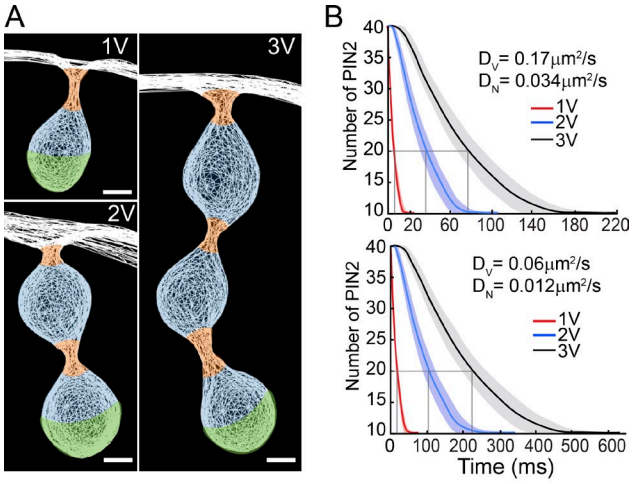

Figure 4. **Simulation of cargo escape in concatenated ILV geometries.** (A) Geometries derived from electron tomograms of plant MVEs used for the cargo diffusion simulations depicted in B. Green indicates the lower ILV hemisphere, where the PIN2 molecules were placed to start the simulation, orange indicates the ILV bud neck and interconnecting membrane bridges, blue indicates the rest of the internalized membrane, and white indicates the endosomal limiting membrane. Bars, 10 nm. (B) Simulated escape times of 40 PIN2 particles placed on the lower hemisphere of the ILV bud using two *D* values (0.06 and 0.17 μm²). The colored lines indicate the mean numbers of remaining cargo over time calculated from >300 simulations, and the shaded regions correspond with the SD. Gray vertical lines indicate the mean times required for 50% of the PIN2 particle to escape the ILV bud. Simulations were run incorporating volume exclusion and a fivefold decrease in *D* when PIN2 particles entered neck or bridge regions (orange in A).

SNF7 as a component of a persistent diffusion barrier on MVE membranes

SNF7 is considered to be the most abundant protein within the ESCRT-III complex and a key component in membrane constriction and ILV formation (Shen et al., 2014; Chiaruttini et al., 2015; Lee et al., 2015). To test whether SNF7 is associated with concatenated ILV buds, we developed antibodies against *Arabidopsis* SNF7 (SNF7.1; Fig. S4 A) and immunolabeled high-pressure–frozen/freeze-substituted roots. We found that SNF7 not only localized to patches on the surface of the endosomal limiting membrane (Fig. S4 B) but also on interconnected ILV buds (Fig. 5, A–C), indicating that ESCRT-III components are associated with ILV bud networks, most likely stabilizing the narrow membrane bridges between vesicles.

ESCRT-III, including SNF7, has been proposed to corral cargo during MVE sorting (Nickerson et al., 2007; Teis et al., 2008; Henne et al., 2012; Chiaruttini et al., 2015) and to be recycled back to the cytoplasm by the time the ILVs are released into the MVE lumen (Babst et al., 2002). Its presence in narrow necks of ILV buds and inter-ILV bridges is consistent with a potential role of SNF7 as a component of a physical barrier for the lateral diffusion of cargo molecules. However, our computational simulations of cargo escape predicted that upon the removal of such a barrier, half of the cargo molecules would escape in 5–20 ms. This prediction, together with our immunogold labeling in Fig. 5 (A–C), strongly argues for the persistence of the hypothetical barrier imposed by SNF7 at the neck and bridge membranes until the physical separation of the ILVs from the limiting membrane. This situation could lead to the complete or partial entrapment of SNF7 in concatenated ILVs and its delivery to the vacuole upon MVE–vacuole fusion. To test this prediction, we isolated protoplasts and vacuoles from wild-type seedlings. We used antibodies against an *Arabidopsis* H⁺PPase to detect vacuolar membranes (Paez-Valencia et al., 2011) and the cytoplasmic FBPase to assess any potential contamination of cytoplasm in the vacuolar fraction (Fig. 5 D). We detected monomeric SNF7 (~25 KD) in both wild-type protoplasts and vacuoles. To rule out that SNF7 had been delivered to the vacuole by autophagy in an MVE-independent fashion, we isolated vacuoles from the *atg7* mutant, which is unable to undergo autophagy of cytoplasmic material (Thompson et al., 2005). We detected comparable amounts of SNF7 in wild-type and *atg7* vacuoles (Fig. 5 D). In contrast, we reasoned that if SNF7 actually remains associated with ILV necks and inter-ILV bridges, as shown by our immunogold labeling and inferred from our modeling, mutants with reduced ILV concatenation would trap less SNF7 in MVEs and therefore deliver less SNF7 to vacuoles. Indeed, as predicted, we detected significantly less SNF7 in vacuoles from *lip5* mutant seedlings compared with those from wild-type control (Fig. 5 D). This observation is consistent with the hypothesis that SNF7 remains associated with ILVs and is trapped inside MVEs once ILVs are released from the limiting membrane.

Finally, to confirm that SNF7 was inside the vacuolar lumen and not associated with the vacuolar surface as a cytoplasmic contaminant, we performed a protease protection assay. Isolated vacuoles were incubated with proteinase K with or without 1% Triton X-100. The anti-H⁺PPase antibody detects an epitope at the lumenal C-terminal tail (Paez-Valencia et al., 2011) that should be protected from the proteinase K treatment in intact vacuoles. We found both SNF7 and the relevant H⁺PPase epitope to be degraded by proteinase K only when Triton X-100 was added (Fig. 5 E), demonstrating that the SNF7 pool detected in the vacuolar fraction is indeed located in the vacuolar lumen.

To explore the effects of a potential ESCRT-imposed cargo diffusion barrier at the membrane-constricted regions of the ILV networks (i.e., necks and inter-ILV bridges), we ran mathematical simulations using the same geometries as in Fig. 4 but applying a retardation factor of 50× and 500× to the two calculated PIN2 diffusion coefficients at the neck- and ILV-interconnecting bridges (Fig. S5). As expected, decreased diffusion at neck and bridge regions led to a delay in cargo escape that was more pronounced for two and three concatenated vesicles than for a one-vesicle geometry, highlighting that multiple diffusion barriers at bridges/necks of an ILV network could be more efficient in trapping cargo than a single diffusion barrier at the neck of a single ILV bud.

Discussion

Our analysis of plant MVEs highlights two important aspects of the robustness and plasticity of the ESCRT machinery across eukaryotes. First, plant MVEs are characterized by a drastically different endosomal membrane geometry and degree of ILV concatenation, which must reflect variation in the relative timing of ESCRT-mediated ILV vesicle formation and membrane fission. Second, this ancestral vesiculation mechanism seems to require that some ESCRT components remain associated with ILVs even after membrane fission, which leads to their entrapment within MVEs and vacuolar degradation.

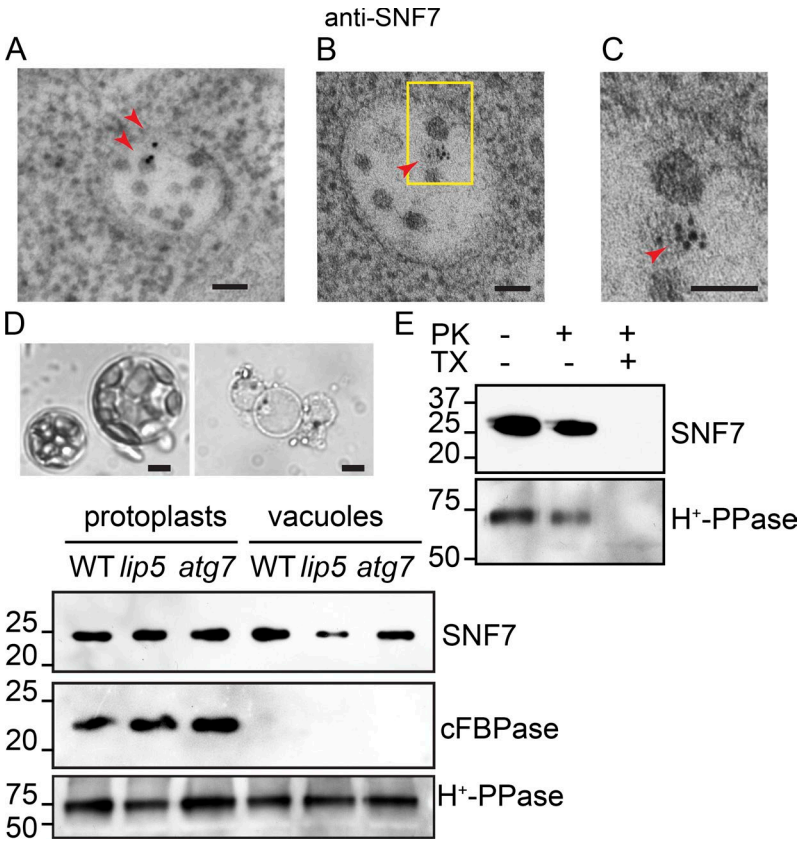

Figure 5. **Detection of SNF7 in MVEs and isolated vacuoles.** (A and B) Immunolabeling of SNF7 on MVEs from high-pressure–frozen/freeze-substituted root cells. (C) The area indicated by a yellow box in B shown at higher magnification. Red arrowheads indicate gold particles. (D) Immunoblot detection of SNF7, cBPPase (cytoplasmic control), and H+PPase (vacuolar membrane control) in protein extracts from isolated protoplasts and vacuoles of wild-type, *lip5*, and *atg7* mutant seedlings. Images of isolated protoplasts and vacuoles are shown at the top. Bars: (A–C) 50 nm; (D) 5 µm. (E) Protease protection assay. Isolated vacuoles were incubated in proteinase K (PK) for 1 h with or without 1% Triton X-100 (TX). SNF7 and H+PPase were detected by immunoblotting. Molecular masses are indicated in kilodaltons.

During ILV formation, the bending of endosomal membranes starts with the recruitment of ESCRT-II and the assembly of the ESCRT-III complex (Fyfe et al., 2011; Adell et al., 2014; Shen et al., 2014; Chiaruttini et al., 2015). As predicted by their behavior on artificial membranes, SNF7 polymers can form spirals of different radii, but they are not small enough to drive membrane fission (Chiaruttini et al., 2015). The binding of VPS4 to ESCRT-III would lead to a remodeling of the ESCRT-III filaments, driving the constriction of the neck of the budding ILV and the subsequent ILV release (Shen et al., 2014; Chiaruttini et al., 2015). However, how neck constriction and membrane scission are temporally regulated remains unknown. The presence of SNF7 in the plant-concatenated ILV networks further supports the idea that stabilization of narrow ILV necks and bridges by SNF7 (and likely other ESCRT components) can be temporally uncoupled from the membrane fission step. This temporal uncoupling leads to a very different geometry of the internalized endosomal membranes that are, nevertheless, able to sequester cargo efficiently.

Other tomographic studies have shown that in yeast and cultured animal cells, all ILVs are free in the MVE lumen (Murk et al., 2003b; Nickerson et al., 2010; Adell et al., 2014). Plants, however, seem to form stable ILV bud networks during MVE sorting. Although plants have overall conserved ESCRT functions, they have also evolved multiple isoforms of conserved ESCRT components and even plant-specific ESCRT proteins (Paez Valencia et al., 2016), which could be responsible for this evolutionary specialization in ILV formation. The capability to form concatenated ILV networks could be related to systems where single ILV release does not proceed fast enough, possibly because of a slower remodeling of the ESCRT-III coat and/or differences in VPS4 kinetics and regulation. It will be interesting to perform structural analyses on MVEs from other multicellular organisms or in different tissues or developmental stages to determine the occurrence and relevance of ILV bud concatenation in other eukaryotic groups.

It is reasonable to speculate that ILV bud concatenation allows endosomes to internalize cargo-containing membrane domains faster than a system in which ILVs are formed one by one. Although our computational simulations suggest a delay in cargo escape as the ILV network becomes more complex, membrane geometry by itself does not seem to impose a diffusion barrier strong enough to prevent cargo escape. Thus, it is reasonable to predict that an additional diffusion barrier must remain in place until membrane fission and ILV release is completed. If ESCRT-III components were to be part of these diffusion barriers at necks and inter-ILV bridges, an immediate corollary is that part of them would be trapped inside MVEs and delivered to vacuoles for degradation. A previous study in yeast proposed that ESCRT-III is recycled back to the cytoplasm and not delivered to the vacuole together with the MVE cargo (Babst et al., 2002). However, we have observed in this study that in plants, SNF7 is detected in ILV networks of MVEs and in the vacuolar lumen. Moreover, as shown by a *lip5* mutation (Fig. 5 D), the amount of SNF7 delivered to the vacuole appears to be correlated with the extent of ILV concatenation. Additionally, other ESCRT-III subunits, such as CHMP1A, VPS24.1, VPS2.1, and ISTL1, have been detected in isolated vacuoles by proteomic approaches (Yoshida et al., 2013), suggesting that SNF7 is not the only ESCRT-III subunit trapped within MVEs and delivered to vacuoles. Thus, we propose that at least in systems with concatenated ILVs, a fraction of SNF7 and likely other ESCRT-III components remain associated with ILV necks

and bridges acting as cargo diffusion barriers even after ILVs lose physical continuity with the limiting membrane.

Materials and methods

Calculations of PIN2 diffusion coefficients

For the FRAP measurements, protoplasts of root tips of 7-d-old seedlings expressing *ProPIN2::PIN2:GFP* were obtained with a modification of a previously described method (Yoo et al., 2007). In brief, root tips were incubated in enzyme solution (20 mM MES, pH 5.7, 0.4 M mannitol, 20 mM KCl, 10 mM $CaCl_2$ containing 1.5% [wt/vol] cellulose R10, and 0.4% [wt/vol] macerozyme R-10) in light for 3 h with mild agitation. Protoplasts were washed in W5 solution (2 mM MES, pH 5.7, 154 mM NaCl, 125 mM $CaCl_2$, and 5 mM KCl) and resuspended in WI solution (4 mM MES, pH 5.7, 0.5 M mannitol, and 20 mM KCl). Protoplasts were visually screened for fluorescence signal. Experiments were performed on an LSM 780 microscope (ZEISS) with a Plan Apochromat 100× 1.46 NA oil differential interference contrast M27 objective with excitation at 488 nm and emission detected between 490–553 nm. To establish the prebleach intensity of the GFP, five images were taken immediately before the bleaching step. A region of interest with a width of 5 µm was bleached on the plasma membrane. Recovery of fluorescence was recorded during 3 min with a delay of 1.40 s between frames. Normalization to prebleach intensity and for loss of fluorescence during imaging was performed as previously described (Phair et al., 2004). The experimental data were analyzed by the equation $I(t) = I(\text{final})(1 - (w^2(w^2 + 4\pi\, Dt)^{-1})^{1/2}$, described by Ellenberg et al. (1997) for strip regions of interest, in which $I(t)$ is intensity as a function of time, I(final) is final intensity reached after complete recovery, w is strip width, and D is diffusion coefficient.

TIRFM imaging was performed using an Elyra PS.1 microscope (ZEISS) with a 100× objective (α Plan Apochromat; 1.46 NA). The gain of the electron-multiplying charge-coupled device camera was set to 300 for all experiments, the setting was within the linear dynamic range of the camera, and images were acquired at 30-ms exposure times. Protoplasts of root tips of plants expressing *Pro35S::PIN2:EosFP* (Dhonukshe et al., 2007) were visually screened for fluorescent signal. To achieve photoconversion at a density compatible with single-particle tracking, a 405-nm laser was used at 0.1% while imaging. The red form of PIN2-EosFP was imaged with 561-nm laser excitation, and fluorescence was collected using a band-pass 570–650 + long-pass 750 filter. Single-particle track segmentation was performed using the TrackMate plugin for Fiji (ImageJ; National Institutes of Health). A total of 648 tracks with a minimum trajectory length of 150 ms and collected from four protoplasts were exported and analyzed with MATLAB using a previously described package for mean square displacement (MSD) analysis (Tarantino et al., 2014) and available at MathWorks. According to this method, we calculated the MSD for each individual trajectory and fitted its log–log representation with a linear function. When the MSD curve can be modeled by $\rho(r) = r^2 = \Gamma ta$, then the $\log(r^2) = f(\log(t))$ is fitted with $\Gamma + \alpha \log(t)$. Those individual MSD curves with an R^2 coefficient <0.8 were discarded.

Modeling and simulation of PIN2 diffusion on the MVE membrane

The PIN2-associated diffusion constant D was directly obtained from experimental measurements. The simulation time step dt depended on the pixel size of the imported MVE geometry and was chosen such that the spatial resolution $s = \sqrt{(4Ddt)}$ of the simulation was guaranteed to be either 0.715 nm or ∼0.226 nm for all values of D. The latter value corresponds to a 10× smaller dt. Based on the presence of 10 predicted transmembrane domains and an intracellular domain, we estimated that a single PIN2 occupies an area of 20 nm^2. Assuming an (idealized) spherical shape for all PIN2 molecules, we obtained a radius r of ∼2.5 nm. This value was required for incorporating volume exclusion effects into PIN2 interaction simulations similar to hard-sphere collision models.

As a unit system, we chose px and ms, yielding different parameter values for geometries with pixel size 0.715 nm and 1.43 nm. Fig. S5 summarizes the chosen time step dt in ms for any given D in $\mu m^2/s$ and px^2/ms.

All simulations of PIN2 diffusion were performed using the computer program Smoldyn (Andrews and Bray, 2004), a particle-based spatial-stochastic simulator. To import the geometries of MVEs (see Figs. 3 and S5), we generated segmentation models of endosomal and ILV membranes using IMOD (Kremer et al., 1996). The files containing meshed objects were first converted into vrml2 format with *imod2vrml2* and then into Smoldyn-readable format using *wrl2smol* from the Smoldyn package. The resulting file was imported into MAT LAB (MathWorks) to manually correct missing triangles and other flaws. Groups of surface triangles within the individual geometries were defined according to their location in the "vesicle bottom" (membrane region furthest away from the endosomal limiting membrane), "neck or bridge" (used for applying a 5× reduction in PIN2 diffusion coefficients), "vesicle" (the remaining surface of the vesicles), and "endosomal limiting membrane" (needed to identify the exit of PIN2) to be used as different Smoldyn surfaces.

Simulations were initialized by uniformly placing 40 PIN2 molecules into the lower hemisphere of the vesicle ("vesicle bottom"). As soon as a PIN2 molecule entered the "endosomal limiting membrane" region, it was permanently removed from the system. To investigate the impact of volume exclusion, we ran simulations using so-called "excluded volume reactions" or "bounce reactions" that efficiently mimic excluded volume behavior by pushing molecules apart that are closer than 2r. We further tested that PIN2 molecules cannot pass each other when diffusing on cylindrical shapes with a radius smaller than 2r. This was to be expected because we had chosen a time step dt that yielded a spatial resolution s that was significantly smaller than 2r. Lastly, numbers of PIN2 were saved at every time step in every simulation. The output file was then imported into and analyzed with MATLAB.

Preparation of anti-SNF7 antibodies

Escherichia coli BL21 cells expressing *Arabidopsis* SNF7.1 fused to GST were grown in 3 ml of Luria-Bertani broth containing kanamycin (50 µg/ml) at 37°C for 3 h, diluted with fresh broth (1:100), and, after 3 h of shaking at 37°C, protein expression was induced by addition of IPTG (0.1 mM final concentration). After 3 h, inclusion bodies containing GST-SNF7 were purified as described previously (Rodríguez-Carmona et al., 2010). In brief, 20 ml of bacterial culture were centrifuged at 5,000 *g* and 4°C for 5 min and resuspended in 20 ml of lysis buffer (50 mM Tris-HCl, pH 8.1, 100 mM NaCl, and 1 mM EDTA) and frozen at −80°C o/n. After thawing, 100 µl of 100-mM PMSF and 400 µl of 50-mg/ml lysozyme were added. After 2 h incubation at 37°C, 100 µl of 0.5% Triton X-100 was added and incubated at room temperature for 1 h. The mixture was then ice jacketed and sonicated between 4 and 10 cycles of 10 min at 40% amplitude under 0.5-s cycles. Then, 5 µl of NP-40 was added to the rest of the suspension, and samples were incubated at 4°C for 1 h. DNA was removed with 15 µl of 1% DNase and 15 µl of 1-M $MgSO_4$ for 45 min at 37°C. Finally, samples were centrifuged at 4°C at 15,000 *g* for 15 min, and the pellet containing inclusion bodies was washed once with 1 ml of lysis buffer containing 0.5% Triton X-100. After a final centrifugation at 15,000 *g* for 15 min at 4°C, pellets were stored at −80°C until analysis. All incubations were done under agitation. The bacterial lysate and purified inclusion bodies were

characterized by electrophoresis in 10% SDS polyacrylamide gel. Proteins were visualized by staining with Coomassie brilliant blue (Bio-Rad Laboratories). Isolated protein bodies were used for production of polyclonal antibodies in rabbits.

For detection of SNF7 proteins in plant extracts, *Arabidopsis* roots were frozen in liquid nitrogen and homogenized in a buffer containing 250 mM sorbitol, 50 mM Hepes–bis-Tris propane (BTP), pH 7.4, 4-(2-hydroxyethyl) piperazine-1-ethanesulfonic acid, *N*-(2-hydroxyethyl) piperazine-*N*′-(2-ethanesulfonic acid) (Sigma-Aldrich), 25 mM ascorbic acid, 1 mM DTT (Fluka), 6 mM EGTA (Sigma-Aldrich), 1.2% (wt/vol) polyvinyl porrolidone-40 (Sigma-Aldrich) and cOmplete protease inhibitor cocktail (Roche). A 1:2 (wt/vol) ratio of tissue and homogenization media was used. The homogenization media was filtered through Miracloth (EMD Millipore) and centrifuged at 10,000 *g* for 15 min. The supernatant was recovered and kept aside. Cleared supernatants were mixed with acetone (1 ml of acetone per 200 µl of cleared homogenate), incubated for 10 min at −20°C, and centrifuged at 20,000 *g* for 10 min. The supernatant was discarded, and the pellet was suspended in 50 µl of a resuspension buffer containing 250 mM sorbitol, 25 mM Hepes-BTP, pH 7.4, 1 mM DTT, and cOmplete EDTA-free protease inhibitor cocktail. Samples were resolved by SDS-PAGE, transferred to nitrocellulose membranes, and analyzed by immunoblotting with the affinity-purified rabbit anti-SNF7.1 via a chemiluminescence detection system (ECL Western blotting substrate; Thermo Fisher Scientific).

Vacuole isolation and protease protection assay

Protoplasts from wild-type Col-0, *atg7*, and *lip5-1* were isolated from a 14-d-old seedling according to Zhai et al. (2009). Intact vacuoles were removed and isolated from protoplasts using thermal and osmotic disruption of the plasma membrane followed by fractionation in a Ficol density gradient (Robert et al., 2007). Isolated vacuoles (50 µg of protein) were resuspended in 100 µl of 10 mM Tris-MES, pH 6.9, and 50 µg of proteinase K with or without 1% Triton X-100 and then were incubated on ice for 1 h (Yamaguchi et al., 2003). TCA was added to terminate the reaction and precipitate proteins. Samples were resolved by SDS-PAGE, transferred to nitrocellulose membranes, and analyzed by immunoblotting with the affinity-purified rabbit anti-SNF7.1, anti-H^+PPase (Paez-Valencia et al., 2011), and cFBPase (AS04043; Agrisera).

Electron microscopy and electron tomography

Roots from 7-d-old *Arabidopsis* seedlings were high-pressure frozen in a BAL-TEC HPM 010 high-pressure freezer. Part of the high-pressure–frozen samples were freeze substituted in 2% OsO_4 in acetone for 12 h at −80°C followed by infiltration in EPON resin (Electron Microscopy Sciences) for structural analysis. Another part of the samples were freeze-substituted in 0.2% glutaraldehyde plus 0.2% uranyl acetate in acetone at −90°C for 4 d in an automated freeze-substitution device (Leica Microsystems) and embedded in Lowicryl HM20 (Electron Microscopy Sciences) for immunolabeling. HM20 sections of HM20-embedded roots were mounted on formvar-coated nickel grids and blocked for 20 min with a 5% (wt/vol) solution of nonfat milk in TBS containing 0.1% Tween-20. The sections were incubated in the primary polyclonal anti-SNF7.1 antibodies for 1 h, rinsed in TBS containing 0.5% Tween-20, and transferred to the secondary antibody (1:10 anti–rabbit IgG) conjugated to either 10- or 6-nm gold particles for 1 h. Controls lacked the primary antibodies.

Sections (300 nm thick) of EPON-embedded roots were mounted on formvar-coated copper slot grids and stained with 2% uranyl acetate in 70% methanol and Reynold's lead citrate (2.6% lead nitrate and 3.5% sodium citrate, pH 12). Colloidal gold particles 15 nm in diameter were used as fiducial markers to align the series of tilted images. The sections were imaged in a Tecnai TF30 intermediate voltage electron microscope (FEI) operated at 300 kV. The images were taken from +60° to –60° at 1.0° intervals about two orthogonal axes (Mastronarde, 1997) and collected in a US1000 camera (Gatan) at a pixel size of 0.715 or 1.43 nm. The images were aligned as described by Ladinsky et al. (1999). Tomograms were computed using simultaneous iterative reconstruction technique (Gilbert, 1972). Merging of the two single-axis tomograms was done as previously described (Mastronarde, 1997). Tomograms were displayed and analyzed with 3Dmod, the graphic component of the IMOD software package (Kremer et al., 1996). The thinning factor for each tomogram was calculated and corrected in the models.

High-pressure–frozen *S. cerevisiae* cells were freeze substituted in 0.25% glutaraldehyde and 0.05% uranyl acetate in acetone at −80°C for 3 d and then at −20°C for one day and then were infiltrated with HM20. Samples were sectioned, and 200-nm-thick sections were placed on formvar-coated copper slot grids and stained with Reynold's lead citrate for 10 min. Fiducial markers of 10 nm gold were placed on both sides of the grid. Tomograms were collected in the same manner as for the *Arabidopsis* roots.

Online supplemental material

Fig. S1 shows *Arabidopsis* MVEs. Fig. S2 shows single-particle tracks collected by TIRFM from a protoplast expressing PIN2-EosFP and used to calculate MSD. Fig. S3 shows cargo diffusion simulations. Fig. S4 shows how SNF7 was detected inside MVEs and vacuoles. Fig. S5 shows simulated escape times of 40 PIN2 particles placed on the lower hemisphere of the ILV bud using two *D* values. Video 1 is a Dual-axis electron tomogram of a wild-type *Arabidopsis* MVE in a cortical root cell. Video 2 is a dual-axis electron tomogram of an MVE in a *lip5 Arabidopsis* root cell. Video 3 is a dual-axis electron tomogram of two *chmp1a chmp1b Arabidopsis* MVEs from a cortical root cell. Video 4 shows photoconverted PIN2-EosFP particles on *Arabidopsis* protoplasts from root tips imaged by TIRFM. Video 5 shows FRAP of PIN2-GFP in *Arabidopsis* protoplasts imaged by confocal microscopy. Video 6 shows simulation of PIN2 particle diffusion in a single ILV budding profile.

Acknowledgments

We thank Bryan Sibert and Christoph Spitzer for processing yeast and *Arabidopsis chmp1* material by high-pressure freezing/freeze substitution, and we thank Anjon Audhya and Gabriele Monshausen for critical reading of the manuscript.

P. Ahlquist is an investigator at the Howard Hughes Medical Institute and the Morgridge Institute for Research. This work was supported by National Science Foundation grants MCB1157824 and MCB1614965 to M.S. Otegui and funds from the University of Wisconsin-Madison Department of Botany to R.A. Buono.

The authors declare no competing financial interests.

Author contributions: R.A. Buono, A. Leier, J. Paez-Valencia, T.T. Marquez-Lago, J. Pennington, K. Goodman, N. Miller, P. Ahlquist, and M.S. Otegui designed research; R.A. Buono, A. Leier, T.T. Marquez-Lago, J. Pennington, and K. Goodman performed research; A. Leier and T.T. Marquez-Lago performed cargo diffusion simulations; R.A. Buono, A. Leier, J. Paez-Valencia, T.T. Marquez-Lago, N. Miller, P. Ahlquist, and M.S. Otegui analyzed data; and A. Leier, T.T. Marquez-Lago, P. Ahlquist, and M.S. Otegui wrote the paper with advice from the other authors.

Submitted: 16 December 2016
Revised: 6 April 2017
Accepted: 1 May 2017

References

Adell, M.A.Y., G.F. Vogel, M. Pakdel, M. Müller, H. Lindner, M.W. Hess, and D. Teis. 2014. Coordinated binding of Vps4 to ESCRT-III drives membrane neck constriction during MVB vesicle formation. *J. Cell Biol.* 205:33–49. http://dx.doi.org/10.1083/jcb.201310114

Andrews, S.S., and D. Bray. 2004. Stochastic simulation of chemical reactions with spatial resolution and single molecule detail. *Phys. Biol.* 1:137–151. http://dx.doi.org/10.1088/1478-3967/1/3/001

Babst, M., D.J. Katzmann, E.J. Estepa-Sabal, T. Meerloo, and S.D. Emr. 2002. Escrt-III: An endosome-associated heterooligomeric protein complex required for mvb sorting. *Dev. Cell.* 3:271–282. http://dx.doi.org/10.1016/S1534-5807(02)00220-4

Bruna, M., and S.J. Chapman. 2012. Excluded-volume effects in the diffusion of hard spheres. *Phys. Rev. E Stat. Nonlin. Soft Matter Phys.* 85:011103. http://dx.doi.org/10.1103/PhysRevE.85.011103

Buono, R.A., J. Paez-Valencia, N.D. Miller, K. Goodman, C. Spitzer, E.P. Spalding, and M.S. Otegui. 2016. Role of SKD1 regulators LIP_5 and IST_1-$LIKE_1$ in endosomal sorting and plant development. *Plant Physiol.* 171:251–264. http://dx.doi.org/10.1104/pp.16.00240

Chiaruttini, N., L. Redondo-Morata, A. Colom, F. Humbert, M. Lenz, S. Scheuring, and A. Roux. 2015. Relaxation of loaded ESCRT-III spiral springs drives membrane deformation. *Cell.* 163:866–879. http://dx.doi.org/10.1016/j.cell.2015.10.017

Dhonukshe, P., F. Aniento, I. Hwang, D.G. Robinson, J. Mravec, Y.D. Stierhof, and J. Friml. 2007. Clathrin-mediated constitutive endocytosis of PIN auxin efflux carriers in *Arabidopsis*. *Curr. Biol.* 17:520–527. http://dx.doi.org/10.1016/j.cub.2007.01.052

Domanov, Y.A., S. Aimon, G.E. Toombes, M. Renner, F. Quemeneur, A. Triller, M.S. Turner, and P. Bassereau. 2011. Mobility in geometrically confined membranes. *Proc. Natl. Acad. Sci. USA.* 108:12605–12610. http://dx.doi.org/10.1073/pnas.1102646108

Ellenberg, J., E.D. Siggia, J.E. Moreira, C.L. Smith, J.F. Presley, H.J. Worman, and J. Lippincott-Schwartz. 1997. Nuclear membrane dynamics and reassembly in living cells: Targeting of an inner nuclear membrane protein in interphase and mitosis. *J. Cell Biol.* 138:1193–1206. http://dx.doi.org/10.1083/jcb.138.6.1193

Fyfe, I., A.L. Schuh, J.M. Edwardson, and A. Audhya. 2011. Association of ESCRT-II with VPS20 generates a curvature-sensitive protein complex capable of nucleating filaments of ESCRT-III. *J. Biol. Chem.* 286:34262–34270. http://dx.doi.org/10.1074/jbc.M111.266411

Ghosh, D., A. Segal, and T. Voets. 2014. Distinct modes of perimembrane TRP channel turnover revealed by TIR-FRAP. *Sci. Rep.* 4:7111. http://dx.doi.org/10.1038/srep07111

Gilbert, P. 1972. Iterative methods for the three-dimensional reconstruction of an object from projections. *J. Theor. Biol.* 36:105–117. http://dx.doi.org/10.1016/0022-5193(72)90180-4

Gomez-Navarro, N., and E.A. Miller. 2016. COP-coated vesicles. *Curr. Biol.* 26:R54–R57. http://dx.doi.org/10.1016/j.cub.2015.12.017

Henne, W.M., N.J. Buchkovich, and S.D. Emr. 2011. The ESCRT pathway. *Dev. Cell.* 21:77–91. http://dx.doi.org/10.1016/j.devcel.2011.05.015

Henne, W.M., N.J. Buchkovich, Y. Zhao, and S.D. Emr. 2012. The endosomal sorting complex ESCRT-II mediates the assembly and architecture of ESCRT-III helices. *Cell.* 151:356–371. http://dx.doi.org/10.1016/j.cell.2012.08.039

Heuser, J.E., and T.S. Reese. 1973. Evidence for recycling of synaptic vesicle membrane during transmitter release at the frog neuromuscular junction. *J. Cell Biol.* 57:315–344. http://dx.doi.org/10.1083/jcb.57.2.315

Hurley, J.H. 2015. ESCRTs are everywhere. *EMBO J.* 34:2398–2407. http://dx.doi.org/10.15252/embj.201592484

Johnson, N., M. West, and G. Odorizzi. 2017. Regulation of yeast ESCRT-III membrane scission activity by the Doa4 ubiquitin hydrolase. *Mol. Biol. Cell.* 28:661–672. http://dx.doi.org/10.1091/mbc.E16-11-0761

Kremer, J.R., D.N. Mastronarde, and J.R. McIntosh. 1996. Computer visualization of three-dimensional image data using IMOD. *J. Struct. Biol.* 116:71–76. http://dx.doi.org/10.1006/jsbi.1996.0013

Ladinsky, M.S., D.N. Mastronarde, J.R. McIntosh, K.E. Howell, and L.A. Staehelin. 1999. Golgi structure in three dimensions: Functional insights from the normal rat kidney cell. *J. Cell Biol.* 144:1135–1149. http://dx.doi.org/10.1083/jcb.144.6.1135

Lee, I.H., H. Kai, L.A. Carlson, J.T. Groves, and J.H. Hurley. 2015. Negative membrane curvature catalyzes nucleation of endosomal sorting complex required for transport (ESCRT)-III assembly. *Proc. Natl. Acad. Sci. USA.* 112:15892–15897. http://dx.doi.org/10.1073/pnas.1518765113

Lee, S.Y., A. Lee, J. Chen, and R. MacKinnon. 2005. Structure of the KvAP voltage-dependent K^+ channel and its dependence on the lipid membrane. *Proc. Natl. Acad. Sci. USA.* 102:15441–15446. http://dx.doi.org/10.1073/pnas.0507651102

Leung, K.F., J.B. Dacks, and M.C. Field. 2008. Evolution of the multivesicular body ESCRT machinery; Retention across the eukaryotic lineage. *Traffic.* 9:1698–1716. http://dx.doi.org/10.1111/j.1600-0854.2008.00797.x

Liu, B., J. Zhang, L. Wang, J. Li, H. Zheng, J. Chen, and M. Lu. 2014. A survey of *Populus* PIN-FORMED family genes reveals their diversified expression patterns. *J. Exp. Bot.* 65:2437–2448. http://dx.doi.org/10.1093/jxb/eru129

MacDonald, C., N.J. Buchkovich, D.K. Stringer, S.D. Emr, and R.C. Piper. 2012. Cargo ubiquitination is essential for multivesicular body intralumenal vesicle formation. *EMBO Rep.* 13:331–338. http://dx.doi.org/10.1038/embor.2012.18

MacDonald, C., J.A. Payne, M. Aboian, W. Smith, D.J. Katzmann, and R.C. Piper. 2015. A family of tetraspans organizes cargo for sorting into multivesicular bodies. *Dev. Cell.* 33:328–342. http://dx.doi.org/10.1016/j.devcel.2015.03.007

Martinière, A., I. Lavagi, G. Nageswaran, D.J. Rolfe, L. Maneta-Peyret, D.-T. Luu, S.W. Botchway, S.E.D. Webb, S. Mongrand, C. Maurel, et al. 2012. Cell wall constrains lateral diffusion of plant plasma-membrane proteins. *Proc. Natl. Acad. Sci. USA.* 109:12805–12810. http://dx.doi.org/10.1073/pnas.1202040109

Mastronarde, D.N. 1997. Dual-axis tomography: An approach with alignment methods that preserve resolution. *J. Struct. Biol.* 120:343–352. http://dx.doi.org/10.1006/jsbi.1997.3919

Murk, J.L.A.N., B.M. Humbel, U. Ziese, J.M. Griffith, G. Posthuma, J.W. Slot, A.J. Koster, A.J. Verkleij, H.J. Geuze, and M.J. Kleijmeer. 2003b. Endosomal compartmentalization in three dimensions: Implications for membrane fusion. *Proc. Natl. Acad. Sci. USA.* 100:13332–13337. http://dx.doi.org/10.1073/pnas.2232379100

Nickerson, D.P., M.R. Russell, and G. Odorizzi. 2007. A concentric circle model of multivesicular body cargo sorting. *EMBO Rep.* 8:644–650. http://dx.doi.org/10.1038/sj.embor.7401004

Nickerson, D.P., M. West, R. Henry, and G. Odorizzi. 2010. Regulators of Vps4 ATPase activity at endosomes differentially influence the size and rate of formation of intralumenal vesicles. *Mol. Biol. Cell.* 21:1023–1032. http://dx.doi.org/10.1091/mbc.E09-09-0776

Obita, T., S. Saksena, S. Ghazi-Tabatabai, D.J. Gill, O. Perisic, S.D. Emr, and R.L. Williams. 2007. Structural basis for selective recognition of ESCRT-III by the AAA ATPase Vps4. *Nature.* 449:735–739. http://dx.doi.org/10.1038/nature06171

Oyola-Cintrón, J., D. Caballero-Rivera, L. Ballester, C.A. Baéz-Pagán, H.L. Martínez, K.P. Vélez-Arroyo, O. Quesada, and J.A. Lasalde-Dominicci. 2015. Lateral diffusion, function, and expression of the slow channel congenital myasthenia syndrome αC418W nicotinic receptor mutation with changes in lipid raft components. *J. Biol. Chem.* 290:26790–26800. http://dx.doi.org/10.1074/jbc.M115.678573

Paez Valencia, J., K. Goodman, and M.S. Otegui. 2016. Endocytosis and endosomal trafficking in plants. *Annu. Rev. Plant Biol.* 67:309–335. http://dx.doi.org/10.1146/annurev-arplant-043015-112242

Paez-Valencia, J., A. Patron-Soberano, A. Rodriguez-Leviz, J. Sanchez-Lares, C. Sanchez-Gomez, P. Valencia-Mayoral, G. Diaz-Rosas, and R. Gaxiola. 2011. Plasma membrane localization of the type I H^+-PPase AVP1 in sieve element–companion cell complexes from *Arabidopsis thaliana*. *Plant Sci.* 181:23–30. http://dx.doi.org/10.1016/j.plantsci.2011.03.008

Pan, Y., S. Wang, Y. Shan, D. Zhang, J. Gao, M. Zhang, S. Liu, M. Cai, H. Xu, G. Li, et al. 2015. Ultrafast tracking of a single live virion during the invagination of a cell membrane. *Small.* 11:2782–2788. http://dx.doi.org/10.1002/smll.201403491

Phair, R.D., S.A. Gorski, and T. Misteli. 2004. Measurement of dynamic protein binding to chromatin in vivo, using photobleaching microscopy. *Methods Enzymol.* 375:393–414. http://dx.doi.org/10.1016/S0076-6879(03)75025-3

Richter, C., M. West, and G. Odorizzi. 2007. Dual mechanisms specify Doa4-mediated deubiquitination at multivesicular bodies. *EMBO J.* 26:2454–2464. http://dx.doi.org/10.1038/sj.emboj.7601692

Richter, C.M., M. West, and G. Odorizzi. 2013. Doa4 function in ILV budding is restricted through its interaction with the Vps20 subunit of ESCRT-III. *J. Cell Sci.* 126:1881–1890. http://dx.doi.org/10.1242/jcs.122499

Robert, S., J. Zouhar, C. Carter, and N. Raikhel. 2007. Isolation of intact vacuoles from Arabidopsis rosette leaf–derived protoplasts. *Nat. Protoc.* 2:259–262. http://dx.doi.org/10.1038/nprot.2007.26

Rodríguez-Carmona, E., O. Cano-Garrido, J. Seras-Franzoso, A. Villaverde, and E. García-Fruitós. 2010. Isolation of cell-free bacterial inclusion bodies. *Microb. Cell Fact.* 9:71. http://dx.doi.org/10.1186/1475-2859-9-71

Rosenberg, M.F., A.B. Kamis, R. Callaghan, C.F. Higgins, and R.C. Ford. 2003. Three-dimensional structures of the mammalian multidrug resistance P-glycoprotein demonstrate major conformational changes in the transmembrane domains upon nucleotide binding. *J. Biol. Chem.* 278:8294–8299. http://dx.doi.org/10.1074/jbc.M211758200

Schuh, A.L., and A. Audhya. 2014. The ESCRT machinery: From the plasma membrane to endosomes and back again. *Crit. Rev. Biochem. Mol. Biol.* 49:242–261. http://dx.doi.org/10.3109/10409238.2014.881777

Shen, Q.T., A.L. Schuh, Y. Zheng, K. Quinney, L. Wang, M. Hanna, J.C. Mitchell, M.S. Otegui, P. Ahlquist, Q. Cui, and A. Audhya. 2014. Structural analysis and modeling reveals new mechanisms governing ESCRT-III spiral filament assembly. *J. Cell Biol.* 206:763–777. http://dx.doi.org/10.1083/jcb.201403108

Spitzer, C., F.C. Reyes, R. Buono, M.K. Sliwinski, T.J. Haas, and M.S. Otegui. 2009. The ESCRT-related CHMP1A and B proteins mediate multivesicular body sorting of auxin carriers in *Arabidopsis* and are required for plant development. *Plant Cell.* 21:749–766. http://dx.doi.org/10.1105/tpc.108.064865

Sundborger, A.C., S. Fang, J.A. Heymann, P. Ray, J.S. Chappie, and J.E. Hinshaw. 2014. A dynamin mutant defines a superconstricted prefission state. *Cell Reports.* 8:734–742. http://dx.doi.org/10.1016/j.celrep.2014.06.054

Tarantino, N., J.Y. Tinevez, E.F. Crowell, B. Boisson, R. Henriques, M. Mhlanga, F. Agou, A. Israël, and E. Laplantine. 2014. TNF and IL-1 exhibit distinct ubiquitin requirements for inducing NEMO-IKK supramolecular structures. *J. Cell Biol.* 204:231–245. http://dx.doi.org/10.1083/jcb.201307172

Teis, D., S. Saksena, and S.D. Emr. 2008. Ordered assembly of the ESCRT-III complex on endosomes is required to sequester cargo during MVB formation. *Dev. Cell.* 15:578–589. http://dx.doi.org/10.1016/j.devcel.2008.08.013

Thompson, A.R., J.H. Doelling, A. Suttangkakul, and R.D. Vierstra. 2005. Autophagic nutrient recycling in Arabidopsis directed by the ATG8 and ATG12 conjugation pathways. *Plant Physiol.* 138:2097–2110. http://dx.doi.org/10.1104/pp.105.060673

Traub, L.M., and J.S. Bonifacino. 2013. Cargo recognition in clathrin-mediated endocytosis. *Cold Spring Harb. Perspect. Biol.* 5:a016790. http://dx.doi.org/10.1101/cshperspect.a016790

Wang, L., A. Dumoulin, M. Renner, A. Triller, and C.G. Specht. 2016. The role of synaptopodin in membrane protein diffusion in the dendritic spine neck. *PLoS One.* 11:e0148310. http://dx.doi.org/10.1371/journal.pone.0148310

Watanabe, S., B.R. Rost, M. Camacho-Pérez, M.W. Davis, B. Söhl-Kielczynski, C. Rosenmund, and E.M. Jorgensen. 2013. Ultrafast endocytosis at mouse hippocampal synapses. *Nature.* 504:242–247. http://dx.doi.org/10.1038/nature12809

Wemmer, M., I. Azmi, M. West, B. Davies, D. Katzmann, and G. Odorizzi. 2011. Bro1 binding to Snf7 regulates ESCRT-III membrane scission activity in yeast. *J. Cell Biol.* 192:295–306. http://dx.doi.org/10.1083/jcb.201007018

Winter, V., and M.-T. Hauser. 2006. Exploring the ESCRTing machinery in eukaryotes. *Trends Plant Sci.* 11:115–123. http://dx.doi.org/10.1016/j.tplants.2006.01.008

Yamaguchi, T., M.P. Apse, H. Shi, and E. Blumwald. 2003. Topological analysis of a plant vacuolar Na^+/H^+ antiporter reveals a luminal C terminus that regulates antiporter cation selectivity. *Proc. Natl. Acad. Sci. USA.* 100:12510–12515. http://dx.doi.org/10.1073/pnas.2034966100

Yoo, S.-D., Y.-H. Cho, and J. Sheen. 2007. *Arabidopsis* mesophyll protoplasts: a versatile cell system for transient gene expression analysis. *Nat. Protoc.* 2:1565–1572. http://dx.doi.org/10.1038/nprot.2007.199

Yoshida, K., M. Ohnishi, Y. Fukao, Y. Okazaki, M. Fujiwara, C. Song, Y. Nakanishi, K. Saito, T. Shimmen, T. Suzaki, et al. 2013. Studies on vacuolar membrane microdomains isolated from Arabidopsis suspension-cultured cells: Local distribution of vacuolar membrane proteins. *Plant Cell Physiol.* 54:1571–1584. http://dx.doi.org/10.1093/pcp/pct107

Zhai, Z., H.I. Jung, and O.K. Vatamaniuk. 2009. Isolation of protoplasts from tissues of 14-day-old seedlings of *Arabidopsis thaliana. J. Vis. Exp.* 30:1149. http://dx.doi.org/10.3791/1149